

# Advancing hierarchical equations of motion for efficient evaluation of coherent two-dimensional spectroscopy

Jian Xu,<sup>1</sup> Rui-Xue Xu,<sup>2,\*</sup> Darius Abramavicius,<sup>3,4</sup> Houdao Zhang,<sup>1</sup> and YiJing Yan<sup>1,2,4,\*</sup>

<sup>1</sup>*Department of Chemistry, Hong Kong University of Science and Technology, Kowloon, Hong Kong SAR, China*

<sup>2</sup>*Hefei National Laboratory for Physical Sciences at the Microscale, University of Science and Technology of China, Hefei, Anhui 230026, China*

<sup>3</sup>*Physics Faculty, Vilnius University, Lithuania and*

<sup>4</sup>*State Key Laboratory of Supramolecular Materials, Jilin University, China*

(Dated: 27 September 2011. Chinese Journal of Chemical Physics, in press)

To advance hierarchical equations of motion as a standard theory for quantum dissipative dynamics, we put forward a mixed Heisenberg–Schrödinger scheme with block-matrix implementation on efficient evaluation of nonlinear optical response function. The new approach is also integrated with optimized hierarchical theory and numerical filtering algorithm. Different configurations of coherent two-dimensional spectroscopy of model excitonic dimer systems are investigated, with focus on the effects of intermolecular transfer coupling and bi-exciton interaction.

## I. INTRODUCTION

Coherent multi-dimensional spectroscopies provide powerful tools to investigate various effects of molecular interactions and dynamic correlations [1–6]. Recent experiments show the evidence of long-lived quantum coherence in photosynthesis systems [7–9], even at room temperatures [10, 11]. Theoretical studies are also carried out towards the simulating and understanding of the involved excitation energy transfer processes [12–17]. In such systems, the pigment-protein interaction has the same magnitude as the pigment-pigment transfer coupling, and the time scale of environment memory is about that of excitation energy transfer. These characteristics require the non-Markovian and non-perturbative quantum dissipation methods. Among them, hierarchical equations of motion (HEOM) approach [18–23], an equivalence to the Feynman-Vernon influence functional path integral [24–26] but numerically more efficient alternative, emerges as a standard method.

There are many recent efforts, in both theoretical and numerical aspects, on advancing exact HEOM to be a power and versatile tool for the study of various quantum dissipative systems. HEOM formalism was originally proposed in 1989 by Tanimura and Kubo for semi-classical dissipation [27]. Formally exact HEOM formalism [18–23] for Gaussian dissipation in general, including its second quantization [28], has now been well established. The major obstacle of HEOM is its numerical tractability. The number of equations involved in the theory are usually huge. Brute-force implementation is greatly limited by both memory and processing capability. One major numerical advancement is the on-the-fly filtering algorithm [29]. It goes with a preselected error tolerance on the properly scaled HEOM. The filtering algorithm dramatically reduces the effective number of

equations, and it by nature also automatically truncates the hierarchy level. In the formulation front, the Padé spectrum decomposition (PSD) scheme [30, 31] has been proposed for an optimized HEOM construction [32]. It dramatically reduces the number of equations, in comparison with that of the conventional Matsubara expansion based formalism at same accuracy. A priori accuracy control criterion has also been proposed [32–34] so that the optimized HEOM can be used confidently, without costly convergence test.

In this work, we discuss two additional techniques to further improve the efficiency of HEOM in evaluating such as the third-order optical response functions and two-dimensional spectroscopy. One is the mixed Heisenberg–Schrödinger scheme. The conventional approach follows the direct realization of third-order response function from the view of Schrödinger picture. It propagates the reduced system density operator in three nested time intervals, denoted as  $t_1$ ,  $t_2$ , and  $t_3$ , between three interrogations and the time of detection which is through dynamic variable such as transition dipole. In the new scheme, while retaining  $t_1$ - and  $t_2$ -propagations on state variables, we unleash  $t_3$  from the nested loop via its propagation in Heisenberg picture on dynamic variables. HEOM in Schrödinger picture and Heisenberg picture are detailed in Sec. II A and Sec. II B, respectively.

Another advancement in this work is the block-HEOM dynamics, for its efficient evaluation of coherent two-dimensional spectroscopy, see Sec. III. In optical processes, the system Hamiltonian is considered to be block diagonalized in electronic manifolds, in virtue of Born-Oppenheimer principle. We also assume that the relaxation between different manifolds is negligible. The resulting HEOM dynamics will be in the block-matrix form, even as they involve in the third-order optical response functions, where the dynamics occur in population and/or coherence states in electronic space. Combining the block-HEOM theory with the mixed Heisenberg–Schrödinger scheme greatly facilitates the evaluation of third-order optical response functions. Moreover, numerical filtering algorithm [29] is now also extended to the

---

\*Electronic address: rxxu@ustc.edu.cn; yyan@ust.hk

present formalism.

We exemplify our method with model excitonic dimer systems in Sec. IV. The well-established  $\mathbf{k}_I$ ,  $\mathbf{k}_{II}$  and  $\mathbf{k}_{III}$  types of coherent two-dimensional spectroscopy [5] are evaluated with the present HEOM dynamics that integrates all the state-of-the-art techniques. Finally we summarize the paper in Sec. V.

## II. HIERARCHICAL EQUATIONS OF MOTION

### A. HEOM in Schrödinger picture

HEOM couples the reduced system density operator of primary interest,  $\rho(t) \equiv \text{tr}_B \rho_{\text{total}}(t)$ , to a set of auxiliary density operators (ADOs). As an exact and nonperturbative theory, HEOM accounts for the combined effects of system-bath coupling strength, environment memory timescales, and many-body interactions [23, 28]. The explicit form of HEOM is defined upon a certain statistical environment bath “basis set” that decomposes the interacting bath correlation functions into distinct memory-frequency components. Without loss of generality, we exemplify it with the case of single-mode system-bath interaction,  $H'(t) = -QF_B(t)$ , where  $Q$  and  $F_B(t)$  are operators in the reduced system and the stochastic bath subspaces, respectively. In general,  $H'(t)$  can be expressed in multiple-modes decomposition form. The stochastic bath operator  $F_B(t)$  assumes a Gaussian process. The influence of bath is therefore described via its correlation function  $C(t) \equiv \langle F_B(t)F_B(0) \rangle_B$ . It is related to the bath spectral density  $J(\omega)$  via the fluctuation-dissipation theorem [25, 35]:

$$C(t) = \frac{1}{\pi} \int_{-\infty}^{\infty} d\omega \frac{e^{-i\omega t} J(\omega)}{1 - e^{-\beta\omega}}, \quad (1)$$

where  $1/(1 - e^{-\beta\omega})$  is Bose function at inverse temperature  $\beta = \hbar/(k_B T)$ . We set  $\hbar = 1$  hereafter.

To construct a HEOM formalism, one need to expand  $C(t)$  in a finite exponential series, on the basis of certain sum-over-poles scheme, together with the Cauchy residue theorem of contour integration applied to Eq. (1). In this work we adopt the Drude model,

$$J(\omega) = \frac{2\lambda\gamma\omega}{\omega^2 + \gamma^2}. \quad (2)$$

In this case,  $[N/N]$  Padé spectrum decomposition (PSD) for Bose function is shown to be the best [30–34]. It results in an exponential expansion of interacting bath correlation function [32],

$$C(t) \approx \sum_{k=0}^N c_k e^{-\gamma_k t} + 2\Delta_N \delta(t), \quad (3)$$

with

$$\Delta_N = \frac{\lambda\beta\gamma}{2(N+1)(2N+3)}. \quad (4)$$

The  $k = 0$  term with  $\gamma_0 \equiv \gamma$  is the Drude pole contribution, while other  $N$  contributions with  $k = 1, \dots, N$  are from the  $[N/N]$  PSD Bose function poles  $\{\gamma_{k \neq 0}\}$  that are all positive and can be easily identified [31]. The  $\delta$ -function term in Eq. (3) re-sums the off-basis-set residue outside the finite sum-over-poles scheme. This is the only approximation involved not just in the bath correlation function, but also in the resulting HEOM that goes therefore by a convenient accuracy control criterion prior to dynamics evaluation [32–34].

The exponential expansion form of  $C(t)$  dictates the construction of HEOM. According to Eq. (3) it reads explicitly as [22, 23, 29, 36]

$$\begin{aligned} \dot{\rho}_n = & - [i\mathcal{L}(t) + \gamma_n + \Delta_N \mathcal{Q}^2] \rho_n \\ & - i \sum_{k=0}^N \sqrt{\frac{n_k}{|c_k|}} (c_k Q \rho_{n_k^-} - c_k^* \rho_{n_k^-} Q) \\ & - i \sum_{k=0}^N \sqrt{(n_k + 1)|c_k|} \mathcal{Q} \rho_{n_k^+}, \end{aligned} \quad (5)$$

with  $\mathcal{L}\rho_n \equiv [H, \rho_n]$  for the reduced system Liouvillian,  $\mathcal{Q}\rho_n \equiv [Q, \rho_n]$ , and

$$\gamma_n = \sum_{k=0}^N n_k \gamma_k. \quad (6)$$

The ADO labeling index is now specified as  $\mathbf{n} \equiv \{n_0, n_1, \dots, n_K\}$ , with  $n_k \geq 0$ . It consists a set of non-negative indices, following the exponential expansion of Eq. (3). The index  $n_k^\pm$  in the last two terms of Eq. (5) differs from  $n$  only by changing the specified  $n_k$  to  $n_k \pm 1$ . Let  $n_0 + n_1 + \dots + n_K = n$  and call the individual  $\rho_n \equiv \rho_{n_0, n_1, \dots, n_K}$  an  $n^{\text{th}}$ -tier ADO. It depends on its associated  $(n \pm 1)^{\text{th}}$ -tier ADOs, specified individually by the last two terms in Eq. (5). The reduced system density operator of primary interest is just the zeroth-tier ADO,  $\rho_0(t) \equiv \rho(t)$ . The  $\Delta_N$ -term in Eq. (5) arises from the white-noise residue in Eq. (3). All ADOs in Eq. (5) are dimensionless and scaled properly to support the efficient HEOM propagator via the on-the-fly filtering algorithm that also automatically truncates the level of hierarchy [29]. The nonperturbative nature of HEOM has been discussed in detail, see Ref. 23 for example. HEOM (5) is called to be in Schrödinger picture, for its governing the system state variables, which are the ADOs including the reduced system density operator of primary interest.

### B. HEOM in Heisenberg picture

HEOM supports the evaluations of not only the expectation values but also the correlation and response functions of any dynamics variables of the reduced system. Nonlinear optical response functions for two-dimensional spectroscopy will be described in the next section. They will be evaluated based on the mixed

Heisenberg–Schrödinger scheme and the block-HEOM dynamics.

Note that HEOM consists a set of linear coupled equations. The HEOM space algebra is mathematically the same of linear space, regardless its physics contents. We recast HEOM as  $\dot{\boldsymbol{\rho}}(t) = -\hat{\mathbf{A}}(t)\boldsymbol{\rho}(t)$ , with the column vector  $\boldsymbol{\rho} \equiv \{\rho_{n=0}, \rho_{n \neq 0}\}$  of ADOs defining a basic element in HEOM space. The dynamic generator  $\hat{\mathbf{A}}(t)$  is determined by specific form of HEOM, i.e. Eq. (5). The HEOM propagator  $\hat{\mathcal{G}}(t, \tau)$  by which  $\boldsymbol{\rho}(t) = \hat{\mathcal{G}}(t, \tau)\boldsymbol{\rho}(\tau)$  satisfies  $\partial\hat{\mathcal{G}}(t, \tau)/\partial t = -\hat{\mathbf{A}}(t)\hat{\mathcal{G}}(t, \tau)$ . In the absence of time-dependent external field,  $\mathcal{L}(t) = \mathcal{L}$  and therefore  $\hat{\mathbf{A}}(t) = \mathbf{A}$  are time-independent, resulting in  $\hat{\mathcal{G}}(t, \tau) = \exp[-\mathbf{A}(t - \tau)] \equiv \mathcal{G}(t - \tau)$ .

The expectation value of a system dynamical variable reads

$$\bar{A} = \text{tr}(A\rho) \equiv \langle\langle A|\rho\rangle\rangle = \langle\langle \mathbf{A}|\boldsymbol{\rho}\rangle\rangle \equiv \sum_{\text{all } n} \langle\langle A_n|\rho_n\rangle\rangle. \quad (7)$$

The first two identities are the conventional reduced Liouville space expressions. The last two identities are the extensions to HEOM space, in which, according to the third identity,

$$\mathbf{A} \equiv \{A_{n=0} = A, A_{n \neq 0} = 0\} = \mathbf{A}(0). \quad (8)$$

The last identity will be used later to specify the initial values of HEOM in Heisenberg picture.

HEOM supports also the evaluation of correlation and response functions. For example, we apply linear response theory to HEOM, resulting in linear correlation function the expression of

$$C_{AB}(t) = \langle\langle \mathbf{A}|\mathcal{G}(t)\overrightarrow{\mathcal{B}}|\boldsymbol{\rho}^{\text{eq}}\rangle\rangle, \quad (9)$$

which is equivalent to  $C_{AB}(t) = \langle\langle A|\mathcal{G}_M(t)|B\rho_M^{\text{eq}}\rangle\rangle = \langle\langle A(t)B(0)\rangle\rangle$ . The latter is the conventional expression, defined in the full system-plus-bath material space. However, Eq. (9) is defined in HEOM space of the reduced system only. The equilibrium  $\boldsymbol{\rho}^{\text{eq}} \equiv \{\rho_{n=0}^{\text{eq}}, \rho_{n \neq 0}^{\text{eq}}\}$  is the stationary solution to HEOM, i.e.  $\mathbf{A}\boldsymbol{\rho}^{\text{eq}} = 0$ , together with the normalization condition of the primary reduced system density operator  $\text{Tr}\rho_0 = 1$ . The resulting  $\{\rho_{n \neq 0}^{\text{eq}} \neq 0\}$  in general account for the initial system-bath correlations. In Eq. (9),  $\overrightarrow{\mathcal{B}}\boldsymbol{\rho}^{\text{eq}} \equiv \{B\rho_{n=0}^{\text{eq}}, B\rho_{n \neq 0}^{\text{eq}}\}$ , in comparison with the full material space counterpart of  $\overrightarrow{B}\rho_M^{\text{eq}} = B\rho_M^{\text{eq}}$ . Denote also  $\overleftarrow{\mathcal{B}}\boldsymbol{\rho} \equiv \{\rho_{n=0}B, \rho_{n \neq 0}B\}$  for later use; cf. Eq. (14).

Apparently, the propagator  $\mathcal{G}(t)$  can take action on a system state variable, e.g.,  $\mathcal{G}(t)\overrightarrow{\mathcal{B}}\boldsymbol{\rho}^{\text{eq}}$  in Eq. (9). This is the Schrödinger picture. It can also act from right to left on a dynamic variable, i.e.,  $\mathbf{A}(t) \equiv \mathbf{A}\mathcal{G}(t)$ . This is the Heisenberg picture, the HEOM analogue of the conventional  $A(t) \equiv A\mathcal{G}_M(t)$  that satisfies the Heisenberg equation,  $\dot{A} = -iA\mathcal{L}_M = -i[A, H_M]$ , defined in the full system-plus-bath material space.

HEOM in Heisenberg picture satisfies  $\dot{\mathbf{A}}(t) = -\mathbf{A}(t)\mathbf{A}$ , with  $\mathbf{A}(0) = \mathbf{A}$  defined in Eq. (8). Its explicit expressions can be obtained as follows. Let us start with the identity,

$$\langle\langle \mathbf{A}|\mathbf{A}|\boldsymbol{\rho}\rangle\rangle = \langle\langle \tilde{\mathbf{A}}|\boldsymbol{\rho}\rangle\rangle = \langle\langle \mathbf{A}|\tilde{\boldsymbol{\rho}}\rangle\rangle, \quad (10)$$

where  $\tilde{\mathbf{A}} \equiv \mathbf{A}\mathbf{A}$  and  $\tilde{\boldsymbol{\rho}} \equiv \mathbf{A}\boldsymbol{\rho}$ , with  $\mathbf{A}$  acting from right and left, respectively. Note that  $\tilde{\mathbf{A}} = -\dot{\mathbf{A}}$  and  $\tilde{\boldsymbol{\rho}} = -\dot{\boldsymbol{\rho}}$ . From Eq. (5) we have

$$\begin{aligned} \langle\langle \mathbf{A}|\tilde{\boldsymbol{\rho}}\rangle\rangle = \sum_{\text{all } n} \left\{ \langle\langle A_n|i\mathcal{L} + \gamma_n + \Delta_N\mathcal{Q}^2|\rho_n\rangle\rangle \right. \\ \left. + i \sum_{k=0}^N \sqrt{\frac{n_k}{|c_k|}} (c_k \langle\langle A_n|Q\rho_{n_k^-}\rangle\rangle - c_k^* \langle\langle A_n|\rho_{n_k^-}Q\rangle\rangle) \right. \\ \left. + i \sum_{k=0}^N \sqrt{(n_k+1)|c_k|} \langle\langle A_n|Q|\rho_{n_k^+}\rangle\rangle \right\}. \quad (11) \end{aligned}$$

In contact with the second quantity in Eq. (10), we recast every individual term above with respect to the same  $\rho_n \equiv \rho_{n_0, n_1, \dots, n_N}$ , by using for example the identity,

$$\sum_{\text{all } n} \sqrt{\frac{n_k}{|c_k|}} \langle\langle A_n|Q\rho_{n_k^-}\rangle\rangle = \sum_{\text{all } n} \sqrt{\frac{n_k+1}{|c_k|}} \langle\langle A_{n_k^+}Q|\rho_n\rangle\rangle.$$

We can therefore recast Eq. (11) as

$$\begin{aligned} \langle\langle \tilde{\mathbf{A}}|\boldsymbol{\rho}\rangle\rangle = \sum_{\text{all } n} \left\{ \langle\langle A_n|i\mathcal{L} + \gamma_n + \Delta_N\mathcal{Q}^2|\rho_n\rangle\rangle \right. \\ \left. + i \sum_{k=0}^N \sqrt{\frac{n_k+1}{|c_k|}} (c_k \langle\langle A_{n_k^+}Q|\rho_n\rangle\rangle - c_k^* \langle\langle Q A_{n_k^+}|\rho_n\rangle\rangle) \right. \\ \left. + i \sum_{k=0}^N \sqrt{n_k|c_k|} \langle\langle A_{n_k^-}|\mathcal{Q}|\rho_n\rangle\rangle \right\}. \end{aligned}$$

Accordingly, HEOM in Heisenberg picture reads explicitly as [37]:

$$\begin{aligned} \dot{\mathbf{A}}_n = -A_n(i\mathcal{L} + \gamma_n + \Delta_N\mathcal{Q}^2) \\ - i \sum_{k=0}^N \sqrt{\frac{n_k+1}{|c_k|}} (c_k A_{n_k^+}Q - c_k^* Q A_{n_k^+}) \\ - i \sum_{k=0}^N \sqrt{n_k|c_k|} A_{n_k^-}Q. \quad (12) \end{aligned}$$

Here,  $\mathcal{O}\mathcal{L} = [O, H]$  and  $\mathcal{O}\mathcal{Q} = [O, Q]$ , following the identities of  $\mathcal{L}\mathcal{O} = [H, O]$  and  $\mathcal{Q}\mathcal{O} = [Q, O]$  defined earlier. Apparently, Eq. (5) and Eq. (12) are equivalent but just in different pictures.

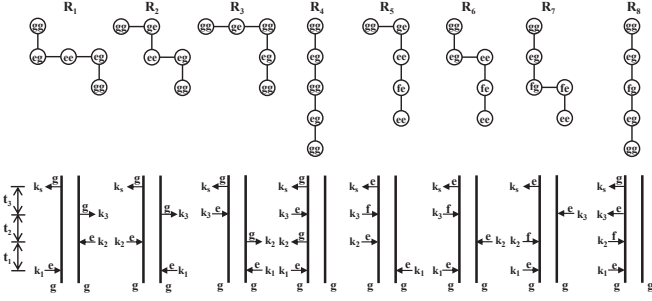


FIG. 1: Eight Liouville-space pathways (upper) and double-sided Feynman diagrams (lower) for two-dimensional spectroscopy in the rotating wave approximation. Each Liouville-space pathway starts from the upper-left circle, while the double-sided Feynman diagram starts from the bottom, following the convention of Ref. 1.

### III. EFFICIENT HEOM EVALUATION OF TWO-DIMENSIONAL SPECTROSCOPIES

#### A. Nonlinear optical response functions via block-HEOM dynamics

Now turn to the third-order optical response functions, as probed by coherent two-dimensional spectroscopies, operated with short pulsed fields in certain four-wave-mixing configurations [2, 5]. Following the similar algebra of the linear correlation/response function, the third-order optical response function in HEOM space is obtained to be

$$R^{(3)}(t_3, t_2, t_1) = \langle\langle \mu_{\mathbf{k}_s} | \mathcal{G}(t_3) \mathcal{D}_{\mathbf{k}_3} \mathcal{G}(t_2) \mathcal{D}_{\mathbf{k}_2} \mathcal{G}(t_1) \mathcal{D}_{\mathbf{k}_1} | \rho^{\text{eq}} \rangle\rangle.$$

It is just the HEOM space analogue of the conventional full system-plus-bath material space expression [1]. Apparently the mixed Heisenberg–Schrödinger scheme as commented in Sec. I will greatly facilitate the evaluation of third-order response function.

As a kind of four-wave-mixing spectroscopy, the wavevector  $\mathbf{k}_s$  of the signal field satisfies the phase-

matching condition. It is that  $\mathbf{k}_s = \pm \mathbf{k}_3 \pm \mathbf{k}_2 \pm \mathbf{k}_1$ , in relation to the three incident pulsed fields interacting with the system sequentially. Three basic configurations of coherent two-dimensional spectroscopy [2, 5] will be classified in Sec. III B. Their efficient evaluation via block-HEOM in mixed Heisenberg–Schrödinger scheme will be detailed in Sec. III C.

In the following, we show that the optical response function can be recast in the block-HEOM dynamics form. Consider the third-order optical processes involving the initial ground  $|g\rangle$ , the excited  $|e\rangle$ , and doubly-excited  $|f\rangle$  manifolds of electronic states. Assume also that the relaxation between different manifolds is negligible. This implies that not only the system Hamiltonian but also the dissipative mode  $Q$  are block diagonalized, in virtue of Born-Oppenheimer principle.

On the other hand, the transition dipole operators involved in the third-order optical response function are also in the block-matrix form, although not diagonal. For example, the transition dipole  $\mu_- \equiv \hat{\mu}_{ge}|g\rangle\langle e| + \hat{\mu}_{ef}|e\rangle\langle f|$  amounts explicitly to

$$\mu_- = \begin{bmatrix} \hat{O}_{gg} & \hat{\mu}_{ge} & \hat{O}_{gf} \\ \hat{O}_{eg} & \hat{O}_{ee} & \hat{\mu}_{ef} \\ \hat{O}_{fg} & \hat{O}_{fe} & \hat{O}_{ff} \end{bmatrix}.$$

The matrix  $\hat{O}_{uv}$  in the  $(uv)$ -block, with  $u, v \in \{g, e, f\}$ , has the order of  $N_u \times N_v$ . We have  $N_g = 1$ ,  $N_e = M$  and  $N_f = M(M-1)/2$ , for a molecular aggregate of size  $M$ , assuming the simple exciton model.

Expanding the third-order optical response function in the eight Liouville-space pathways, as shown in Fig. 1, and their complex conjugate counterparts leads to [1, 38]

$$R^{(3)}(t_3, t_2, t_1) = i^3 \sum_{\alpha=1}^8 [R_\alpha(t_3, t_2, t_1) - \text{c.c.}]. \quad (13)$$

These eight pathways contributions are expressed in terms of the block-matrix dynamics in HEOM space as

$$\begin{aligned} R_1(t_3, t_2, t_1) &= \langle\langle \mu_{ge} | \mathcal{G}_{eg}(t_3) \overleftarrow{\mu}_{eg} \mathcal{G}_{ee}(t_2) \overleftarrow{\mu}_{ge} \mathcal{G}_{eg}(t_1) \overrightarrow{\mu}_{eg} | \rho_{gg}^{\text{eq}} \rangle\rangle e^{-i\omega_{eg}(t_3+t_1)}, \\ R_2(t_3, t_2, t_1) &= \langle\langle \mu_{ge} | \mathcal{G}_{eg}(t_3) \overleftarrow{\mu}_{eg} \mathcal{G}_{ee}(t_2) \overrightarrow{\mu}_{eg} \mathcal{G}_{ge}(t_1) \overleftarrow{\mu}_{ge} | \rho_{gg}^{\text{eq}} \rangle\rangle e^{-i\omega_{eg}(t_3-t_1)}, \\ R_3(t_3, t_2, t_1) &= \langle\langle \mu_{ge} | \mathcal{G}_{eg}(t_3) \overrightarrow{\mu}_{eg} \mathcal{G}_{gg}(t_2) \overleftarrow{\mu}_{eg} \mathcal{G}_{ge}(t_1) \overleftarrow{\mu}_{ge} | \rho_{gg}^{\text{eq}} \rangle\rangle e^{-i\omega_{eg}(t_3-t_1)}, \\ R_4(t_3, t_2, t_1) &= \langle\langle \mu_{ge} | \mathcal{G}_{eg}(t_3) \overrightarrow{\mu}_{eg} \mathcal{G}_{gg}(t_2) \overrightarrow{\mu}_{ge} \mathcal{G}_{eg}(t_1) \overrightarrow{\mu}_{eg} | \rho_{gg}^{\text{eq}} \rangle\rangle e^{-i\omega_{eg}(t_3+t_1)}, \\ R_5(t_3, t_2, t_1) &= -\langle\langle \mu_{ef} | \mathcal{G}_{fe}(t_3) \overrightarrow{\mu}_{fe} \mathcal{G}_{ee}(t_2) \overrightarrow{\mu}_{eg} \mathcal{G}_{ge}(t_1) \overleftarrow{\mu}_{ge} | \rho_{gg}^{\text{eq}} \rangle\rangle e^{-i(\omega_{fe}t_3 - \omega_{eg}t_1)}, \\ R_6(t_3, t_2, t_1) &= -\langle\langle \mu_{ef} | \mathcal{G}_{fe}(t_3) \overrightarrow{\mu}_{fe} \mathcal{G}_{ee}(t_2) \overleftarrow{\mu}_{ge} \mathcal{G}_{eg}(t_1) \overrightarrow{\mu}_{eg} | \rho_{gg}^{\text{eq}} \rangle\rangle e^{-i(\omega_{fe}t_3 + \omega_{eg}t_1)}, \\ R_7(t_3, t_2, t_1) &= -\langle\langle \mu_{ef} | \mathcal{G}_{fe}(t_3) \overleftarrow{\mu}_{ge} \mathcal{G}_{fg}(t_2) \overrightarrow{\mu}_{fe} \mathcal{G}_{eg}(t_1) \overrightarrow{\mu}_{eg} | \rho_{gg}^{\text{eq}} \rangle\rangle e^{-i(\omega_{fe}t_3 + \omega_{fg}t_2 + \omega_{eg}t_1)}, \\ R_8(t_3, t_2, t_1) &= \langle\langle \mu_{ge} | \mathcal{G}_{eg}(t_3) \overrightarrow{\mu}_{ef} \mathcal{G}_{fg}(t_2) \overrightarrow{\mu}_{fe} \mathcal{G}_{eg}(t_1) \overrightarrow{\mu}_{eg} | \rho_{gg}^{\text{eq}} \rangle\rangle e^{-i(\omega_{eg}t_3 + \omega_{fg}t_2 + \omega_{eg}t_1)}. \end{aligned} \quad (14)$$

The underlying optical processes will be discussed in Sec. III B. The electronic phase factor in each individual  $R_\alpha$  can be formally absorbed into the involving Green's functions, i.e.,  $\mathcal{G}_{uv}(t)e^{-i\omega_{uv}t} \rightarrow \mathcal{G}_{uv}(t)$ , with  $\omega_{uv} \equiv \epsilon_u - \epsilon_v$  denoting the chosen reference frequency for the optical transition between two specified electronic manifolds. In the present notion,  $\mathcal{G}_{uv}(t)$  involves only slow motion dynamics, as the highly oscillatory optical frequency component is factorized out for numerical advantage. The corresponding block HEOM dynamics in both Schrödinger and Heisenberg pictures will be detailed in Sec. III C. There are other advantages for the present notion. The overall electronic phase factor can in fact be used to distinguish rephasing versus non-rephasing optical processes [1, 38, 39] and also to visualize the rotating wave approximation as seen below.

### B. Coherent two-dimensional spectroscopies

There are three basic configurations of coherent two-dimensional spectroscopy, and their signals are denoted as  $S_{\mathbf{k}_I}$ ,  $S_{\mathbf{k}_{II}}$ , and  $S_{\mathbf{k}_{III}}$ , respectively [5]. For simplicity we adopt the rotating-wave approximation and the impulsive fields limit.

The  $S_{\mathbf{k}_I}$  signal goes with  $\mathbf{k}_s = \mathbf{k}_3 + \mathbf{k}_2 - \mathbf{k}_1$ , the stimulated photon echo or rephasing configuration [39], while the  $S_{\mathbf{k}_{II}}$  signal goes with  $\mathbf{k}_s = \mathbf{k}_3 - \mathbf{k}_2 + \mathbf{k}_1$  and is non-rephasing. With the aid of the double-sided Feynman diagrams in Fig. 1, these two signals are identified to be

$$S_{\mathbf{k}_{I/II}}(\omega_3, t_2, \omega_1) = \text{Re} \int_0^\infty dt_3 \int_0^\infty dt_1 e^{i(\omega_3 t_3 \mp \omega_1 t_1)} \times R_{\mathbf{k}_{I/II}}(t_3, t_2, t_1), \quad (15)$$

and related respectively to

$$\begin{aligned} R_{\mathbf{k}_I} &= R_2 + R_3 + R_5 && \text{(rephasing)}, \\ R_{\mathbf{k}_{II}} &= R_1 + R_4 + R_6 && \text{(non-rephasing)}. \end{aligned} \quad (16)$$

The rephasing versus non-rephasing nature of individual  $R_\alpha$  in Eq. (14) or Eq. (16) can be inferred easily from its overall electronic phase factor [1, 38, 39]. The signs associating with the frequencies  $\omega_3$  and  $\omega_1$  in Eq. (15) are resulted from the incident fields in the specified four wave mixing configuration in the impulsive limit, as implied in Fig. 1. These signs are just opposite to those in the electronic phase factor of participating  $R_\alpha$  contributions. Thus, the participated pathway contributions via the electronic rotating wave approximation are also evident in Eq. (15).

Experiments can also be performed in the configuration that the pulsed  $\mathbf{k}_2$ -field is applied continuously not only after but also before the  $\mathbf{k}_1$ -field. The resulting signal amounts to  $S_{\mathbf{k}_I + \mathbf{k}_{II}} = S_{\mathbf{k}_I} + S_{\mathbf{k}_{II}}$ . It is in fact the pump-probe absorption configuration, involving all the six pathways  $R_1$  to  $R_6$  contributions. As inferred from Eq. (14), these six pathways can be classified into

the *excited-state emission* ( $R_1, R_2$ ), *ground-state bleaching* ( $R_3, R_4$ ), and *excited-state absorption* ( $R_5, R_6$ ) contributions. In fact, the  $t_1$  and  $t_3$  represent the excitation and detection time periods, and therefore, the  $\omega_1$  and  $\omega_3$  in Eq. (15) are the excitation and detection frequencies, respectively. The  $t_2$  denotes the waiting time, during which the system is either in the excited or the ground state manifold, with underlying dynamics being governed by  $\mathcal{G}_{ee}(t_2)$  or  $\mathcal{G}_{gg}(t_2)$ , respectively; see Eq. (14).

The  $S_{\mathbf{k}_{III}}$  signal goes with  $\mathbf{k}_s = -\mathbf{k}_3 + \mathbf{k}_2 + \mathbf{k}_1$ , the double-excitation configuration, and is related to

$$R_{\mathbf{k}_{III}} = R_7 + R_8, \quad (17)$$

as inferred from the double-sided Feynman diagrams in Fig. 1. The  $R_7$  and  $R_8$  are the *double-excitation absorption* pathways, involving the  $|f\rangle \leftarrow |e\rangle \leftarrow |g\rangle$  processes, while the bra state remains in  $\langle g|$ . During the time  $t_2$  period, the  $\mathbf{k}_{III}$  configuration explores therefore double quantum coherence dynamics governed by  $\mathcal{G}_{fg}(t_2)$ , in contrast to the  $\mathbf{k}_{I/II}$  scheme involving electronic state population dynamics. The detection  $\mathbf{k}_3$  field involves single-excitation absorption of  $\langle e| \leftarrow \langle g|$  in  $R_7$  and single-excitation emission  $|e\rangle \leftarrow |f\rangle$  in  $R_8$ , as evident in the corresponding double-sided Feynman diagrams in Fig. 1. The above analysis justifies the fact that the  $\mathbf{k}_{III}$ -signal is designed to probe the correlation between single and double excitations [15, 40, 41]. The two-dimensional half-Fourier transforms are therefore performed with  $t_2$  to resolve the double-excitation frequency and with either  $t_3$  or  $t_1$  to resolve the specified single-excitation frequency. In this work, we choose

$$S_{\mathbf{k}_{III}}(\omega_3, \omega_2, t_1) = \text{Re} \int_0^\infty dt_3 \int_0^\infty dt_2 e^{i(\omega_3 t_3 + \omega_2 t_2)} \times R_{\mathbf{k}_{III}}(t_3, t_2, t_1). \quad (18)$$

In the independent exciton limit, the  $\mathbf{k}_{III}$ -signal vanishes. This can be seen from the involving  $R_7$  and  $R_8$  contributions [cf. Eq. (14)]. Besides the signs, these two contributions differ by their single coherence dynamics in the  $t_3$  period, which is  $\mathcal{G}_{fe}(t_3)$  in  $R_7$  but  $\mathcal{G}_{eg}(t_3)$  in  $R_8$ . These two contributions would cancel each other in the absence of both inter-exciton transfer coupling and double-exciton correlation. Thus the  $\mathbf{k}_{III}$  technique serves as a sensitive probe for interactions between excitons.

### C. Implementation with block-HEOM in mixed Heisenberg–Schrödinger picture

To implement the third order optical response functions in Eq. (14), we start with the thermal equilibrium  $\rho_{gg}^{\text{eq}}$  in the ground-state  $|g\rangle$ -manifold. As described earlier, it is determined by the steady state solution to HEOM, involving now only the  $(gg)$ -block part. For the simple exciton model, the  $|g\rangle$ -manifold contains only one level, and the ADOs in  $(gg)$ -block are all  $1 \times 1$  matrices, resulting in  $\rho_{gg}^{\text{eq}} = \{\rho_{n=0}^{gg, \text{eq}} = 1, \rho_{n \neq 0}^{gg, \text{eq}} = 0\}$ .

Block-matrix multiplications are then followed:

$$\vec{\mu}_{eg}\rho_{gg}^{\text{eq}} = \{\hat{\mu}_{eg}\rho_{n=0}^{gg,\text{eq}}, \hat{\mu}_{eg}\rho_{n\neq 0}^{gg,\text{eq}}\} \equiv \tilde{\rho}_{eg}(0). \quad (19)$$

Denote also  $\tilde{\rho}_{ge}(0) \equiv \overleftarrow{\mu}_{ge}\rho_{gg}^{\text{eq}} = \{\rho_{n=0}^{gg,\text{eq}}\hat{\mu}_{ge}, \rho_{n\neq 0}^{gg,\text{eq}}\hat{\mu}_{ge}\}$ . They are the initial states for the block-HEOM  $\mathcal{G}_{uv}(t_1)$  propagations in Eq. (14). Each ADO in  $\tilde{\rho}_{uv}$  is an  $N_u \times N_v$  matrix, as inferred in the  $(uv)$ -indexes, and also Hermite conjugate with its counterpart in  $\tilde{\rho}_{vu}$ ; i.e.,  $\tilde{\rho}_{vu} = \{\tilde{\rho}_{uv}^\dagger\} \equiv \tilde{\rho}_{uv}^\dagger$ .

The  $t_1$ - and  $t_2$ -propagations in Eq. (14) are implemented in a nested manner in Schrödinger picture. This picture is defined via the action-from-left of  $\mathcal{G}_{uv}(t)$  on state variables; e.g.,  $\tilde{\rho}_{uv}(t) = \mathcal{G}_{uv}(t)\tilde{\rho}_{uv}(0)$ . The block-HEOM in Schrödinger picture can be reduced from Eq. (5) as

$$\begin{aligned} \dot{\rho}_n^{uv} = & -i(\mathcal{L}_{uv} + \gamma_n + \Delta_N \mathcal{Q}_{uv}^2)\tilde{\rho}_n^{uv} \\ & -i \sum_{k=0}^N \sqrt{\frac{n_k}{|c_k|}} (c_k Q_{uu}\tilde{\rho}_{n_k}^{uv} - c_k^* \tilde{\rho}_{n_k}^{uv} Q_{vv}) \\ & -i \sum_{k=0}^N \sqrt{(n_k+1)|c_k|} Q_{uv}\tilde{\rho}_{n_k^+}^{uv}. \end{aligned} \quad (20)$$

Here,  $\mathcal{L}_{uv}\hat{O}_{uv} \equiv H_{uu}\hat{O}_{uv} - \hat{O}_{uv}H_{vv}$  and  $\mathcal{Q}_{uv}\hat{O}_{uv} \equiv Q_{uu}\hat{O}_{uv} - \hat{O}_{uv}Q_{vv}$ . Equivalently,  $\hat{O}_{vu}\mathcal{L}_{uv} = \hat{O}_{vu}H_{uu} - H_{vv}\hat{O}_{vu}$  and  $\hat{O}_{vu}\mathcal{Q}_{uv} = \hat{O}_{vu}Q_{uu} - Q_{vv}\hat{O}_{vu}$ , which will be used in the following Heisenberg picture.

The  $t_3$ -propagation in Eq. (14) is implemented in Heisenberg picture, in parallel with the  $t_1$ - and  $t_2$ -propagations. The Heisenberg picture is defined via the action-from-right of  $\mathcal{G}_{uv}(t)$  on dynamic variables, i.e.,  $\mathbf{A}_{vu}(t) = \mathbf{A}_{vu}\mathcal{G}_{uv}(t)$ . The initial condition is  $\mathbf{A}_{vu}(0) = \mathbf{A}_{vu} = \{\mathbf{A}_{n=0}^{vu} = \mathbf{A}_{vu}, \mathbf{A}_{n\neq 0}^{vu} = 0\}$ , following Eq. (8). In consistent with Eq. (20) or Eq. (12), the block-HEOM in Heisenberg picture reads

$$\begin{aligned} \dot{\mathbf{A}}_n^{vu} = & -i\mathbf{A}_n^{vu}(\mathcal{L}_{uv} + \gamma_n + \Delta_N \mathcal{Q}_{uv}^2) \\ & -i \sum_{k=0}^N \sqrt{\frac{n_k+1}{|c_k|}} (c_k \mathbf{A}_{n_k^+}^{vu} Q_{uu} - c_k^* Q_{vv} \mathbf{A}_{n_k^+}^{vu}) \\ & -i \sum_{k=0}^N \sqrt{n_k |c_k|} \mathbf{A}_{n_k^-}^{vu} Q_{uv}. \end{aligned} \quad (21)$$

To evaluate the third-order optical response functions in Eq. (14) with block-HEOM in mixed Heisenberg–Schrödinger scheme, we introduce

$$\tilde{\rho}_{uv}(t_2; t_1) \equiv \mathcal{G}_{uv}(t_2)\tilde{\rho}_{uv}(0; t_1), \quad (22)$$

for three types of initial  $t_2$  conditions:

$$\begin{aligned} \tilde{\rho}_{ee}(0; t_1) & \equiv \overleftarrow{\mu}_{ge}\tilde{\rho}_{eg}(t_1), \\ \tilde{\rho}_{gg}(0; t_1) & \equiv \overrightarrow{\mu}_{ge}\tilde{\rho}_{eg}(t_1), \\ \tilde{\rho}_{fg}(0; t_1) & \equiv \overrightarrow{\mu}_{fe}\tilde{\rho}_{eg}(t_1). \end{aligned} \quad (23)$$

We can recast Eq. (14) as (up to the phase factors)

$$\begin{aligned} R_1(t_3, t_2, t_1) & = \langle\langle \mu_{ge}(t_3) | \overleftarrow{\mu}_{eg}\tilde{\rho}_{ee}(t_2; t_1) \rangle\rangle, \\ R_2(t_3, t_2, t_1) & = \langle\langle \mu_{ge}(t_3) | \overleftarrow{\mu}_{eg}\tilde{\rho}_{ee}^\dagger(t_2; t_1) \rangle\rangle, \\ R_3(t_3, t_2, t_1) & = \langle\langle \mu_{ge}(t_3) | \overrightarrow{\mu}_{eg}\tilde{\rho}_{gg}^\dagger(t_2; t_1) \rangle\rangle, \\ R_4(t_3, t_2, t_1) & = \langle\langle \mu_{ge}(t_3) | \overrightarrow{\mu}_{eg}\tilde{\rho}_{gg}(t_2; t_1) \rangle\rangle, \\ R_5(t_3, t_2, t_1) & = -\langle\langle \mu_{ef}(t_3) | \overrightarrow{\mu}_{fe}\tilde{\rho}_{ee}^\dagger(t_2; t_1) \rangle\rangle, \\ R_6(t_3, t_2, t_1) & = -\langle\langle \mu_{ef}(t_3) | \overrightarrow{\mu}_{fe}\tilde{\rho}_{ee}(t_2; t_1) \rangle\rangle, \\ R_7(t_3, t_2, t_1) & = -\langle\langle \mu_{ef}(t_3) | \overleftarrow{\mu}_{ge}\tilde{\rho}_{fg}(t_2; t_1) \rangle\rangle, \\ R_8(t_3, t_2, t_1) & = \langle\langle \mu_{ge}(t_3) | \overrightarrow{\mu}_{ef}\tilde{\rho}_{fg}(t_2; t_1) \rangle\rangle. \end{aligned} \quad (24)$$

These are the final expressions for the mixed Heisenberg–Schrödinger scheme block-HEOM evaluation of third-order optical response functions and coherent two-dimensional spectrums via such as Eqs. (15) and (18).

We have also successfully extended the on-the-fly filtering algorithm [29] to the block-HEOM dynamics in Eq. (24). There involve the nested  $(t_2; t_1)$ -propagation in Schrödinger picture [Eq. (20)] and the separated  $t_3$ -propagation in Heisenberg picture [Eq. (21)]. Setting the filtering error tolerance at  $2 \times 10^{-5}$  is found to be sufficient for HEOM dynamics in both Schrödinger and Heisenberg pictures, as tested extensively on various systems, with numerical accuracy by eyes.

#### IV. NUMERICAL DEMONSTRATIONS

We exemplify the efficient evaluation of coherent two-dimensional spectrums with a model excitonic dimer. Its Hamiltonian reads

$$H = \epsilon_1 \hat{b}_1^\dagger \hat{b}_1 + \epsilon_2 \hat{b}_2^\dagger \hat{b}_2 + V(\hat{b}_1^\dagger \hat{b}_2 + \hat{b}_2^\dagger \hat{b}_1) + U \hat{b}_1^\dagger \hat{b}_1 \hat{b}_2^\dagger \hat{b}_2,$$

where  $\hat{b}_m^\dagger$  ( $\hat{b}_m$ ) denotes the exciton creation (annihilation) operator on the specified molecular site. The model system consists of a total four levels:  $|g\rangle = |00\rangle$  in the ground-state manifold,  $|e\rangle = |10\rangle$  and  $|01\rangle$  in the single-exciton manifold, and  $|f\rangle = |11\rangle$  in the double-exciton manifold. The Rabi frequency within the single-exciton manifold is  $\sqrt{(\epsilon_1 - \epsilon_2)^2 + 4V^2}$ . The electronic transition dipoles  $\mu_{eg} = (\mu_1|10\rangle + \mu_2|01\rangle)\langle 00|$  and  $\mu_{fe} = |11\rangle(\langle 10|\mu_2 + \langle 01|\mu_1)$ . Co-linear ( $xxx$ ) field polarization configuration is adopted, so that the effect of dipole directions on spectroscopic signals can be neglected.

Each on-site transition energy experiences fluctuations, brought in through  $Q_m = \hat{b}_m^\dagger \hat{b}_m$  influence of bath in Drude model. We neglect the cross correlation between different on-site fluctuations, and also the static disorders that are irrelevant to the methodology of this work. In the following, we set  $\lambda = 60 \text{ cm}^{-1}$  and  $\gamma^{-1} = 100 \text{ fs}$  for each individual on-site Drude dissipation [Eq. (2)] and 77 K for temperature. In all cases, the [1/1]-PSD scheme is sufficient according to the established accuracy control criterion [32–34].

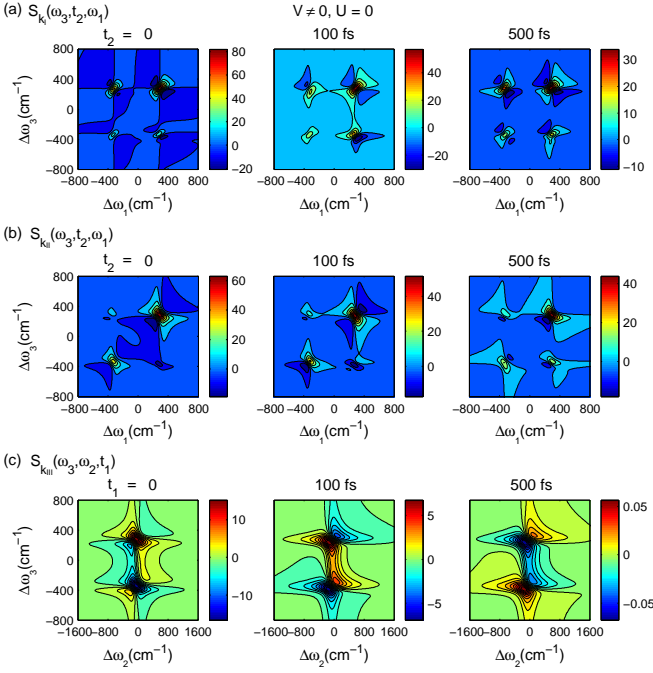


FIG. 2: Coherent two-dimensional spectra for the dimer system:  $\epsilon_1 = \epsilon_2 = \epsilon$ ,  $V = -300 \text{ cm}^{-1}$ , and  $U = 0$ , with  $\mu_1/\mu_2 = -5$ , at temperature 77 K. Drude dissipation parameters for each on-site excitation energy fluctuation are  $\lambda = 60 \text{ cm}^{-1}$  and  $\gamma^{-1} = 100 \text{ fs}$ . Frequencies (when applicable) are reported in terms of  $\Delta\omega_1 = \omega_1 - \epsilon$ ,  $\Delta\omega_3 = \omega_3 - \epsilon$  and  $\Delta\omega_2 = \omega_2 - 2\epsilon$ , as the electronic reference transition frequencies are chosen to be  $\omega_{eg} = \omega_{fe} = \epsilon$  and  $\omega_{fg} = 2\epsilon$ .

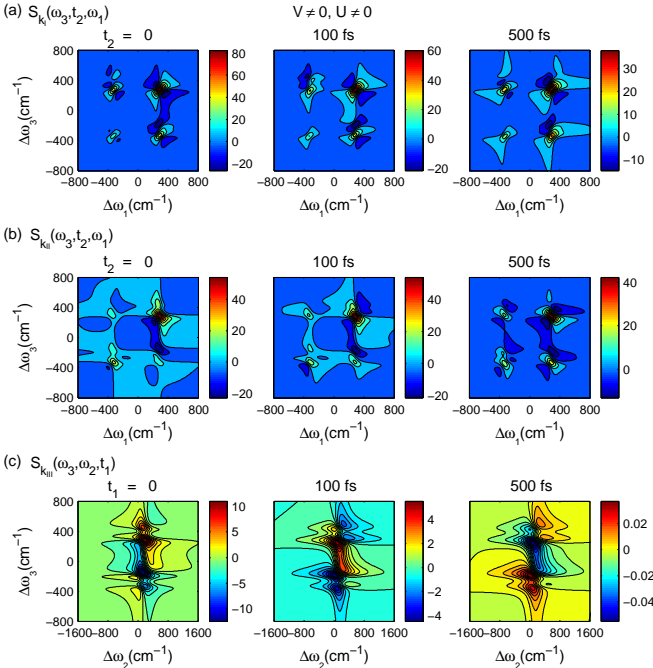


FIG. 3: Same as Fig. 2 but with a finite bi-exciton interaction,  $U = 200 \text{ cm}^{-1}$ .

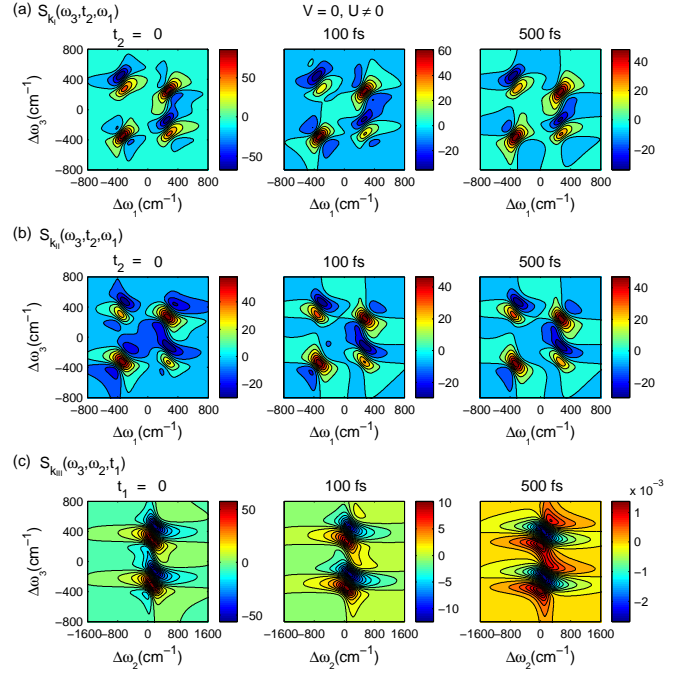


FIG. 4: Same as Fig. 3 but for  $\epsilon_1 = \epsilon - 300 \text{ cm}^{-1}$ ,  $\epsilon_2 = \epsilon + 300 \text{ cm}^{-1}$ , and  $V = 0$ , with  $\mu_1/\mu_2 = 1$ .

Figures 2–4 exemplify three representative cases of ( $V \neq 0, U = 0$ ), ( $V \neq 0, U \neq 0$ ), and ( $V = 0, U \neq 0$ ), respectively, but sharing a common value of Rabi frequency  $\sqrt{(\epsilon_1 - \epsilon_2)^2 + 4V^2}$ . Thus the peaks and valleys, which reflect the transition frequencies between nonlocal eigenstates, are distributed at similar positions in these three figures. Highlighted are therefore the effects of excitonic transfer coupling  $V$  and bi-exciton interaction  $U$  on  $S_{\mathbf{k}_I}$ ,  $S_{\mathbf{k}_{II}}$ , and  $S_{\mathbf{k}_{III}}$ , as depicted in the panels (a), (b) and (c) of each individual figure. Intensities are reported in their relative values, with a common factor over all frames in these figures.

General speaking, both  $V$  and  $U$  affect correlations between different monomers, manifested via the cross peaks in  $S_{\mathbf{k}_I}$  and  $S_{\mathbf{k}_{II}}$ . On the other hand,  $S_{\mathbf{k}_{III}}$  that vanishes when  $U = V = 0$  is specialized for the correlation between single and double excitation coherence. It provides a different way to visualize the effects of finite  $U$  and/or  $V$ , as evident from Figs. 2–4. The presence of  $U$  manifests mainly on the separation of peaks and valleys (cf. Fig. 4 for example) and it is particularly prominent in the  $S_{\mathbf{k}_{III}}$  spectrum.

Other observations in rephasing  $S_{\mathbf{k}_I}$  and non-rephasing  $S_{\mathbf{k}_{II}}$  are briefed as follows: (i) The peaks arise from excited state emission ( $R_2$  and  $R_1$ ) and ground state bleaching ( $R_3$  and  $R_4$ ), while the valleys are from excited state absorption ( $R_5$  and  $R_6$ ); (ii) The peaks/valleys are along the diagonal direction in  $S_{\mathbf{k}_I}$  and anti-diagonal in  $S_{\mathbf{k}_{II}}$ , in line with Eq. (15). Inhomogeneity that is not included in calculations affects mainly the diagonal direction. Thus, it elongates the diagonal peaks in  $S_{\mathbf{k}_I}$ , while smears those

in  $S_{\mathbf{k}_{II}}$ ; (iii) Bi-exciton interaction  $U$  shifts the excited state absorption, with respect to the excited state emission and ground state bleaching. These two components differ in signs, being of valley versus peak. Thus, cancellation would occur at least partially when  $U = 0$ ; (iv) Excitation energy transfer is observed as the evolution of peaks/valleys intensities. This process is mainly responsible by  $V \neq 0$ ; (v) The correlation effects arising from  $U$  are separated out in Fig. 4. The negative peaks in Fig. 4 (a) and (b) would cancel completely with the positive ones when  $U = 0$ . The larger the  $U$  is, the bluer shift of the negative peaks from their positive counterparts. Note that the dimer system studied in Fig. 4 is nondegenerate, rather than the degenerate ones in Figs. 2 and 3, for the appearance of correlation and coherence between two distinct monomers.

## V. CONCLUDING REMARKS

In summary, we propose a mixed Heisenberg–Schrödinger scheme and block-HEOM theory, and

demonstrate it with efficient evaluation of third-order optical response function and coherent two-dimensional spectroscopy. The new development has also been integrated with the efficient numerical filtering algorithm [29] and the optimized hierarchical theory [32–34]. This is the state-of-the-art HEOM approach. For example, the calculations of all frames in Fig. 2 take only about three minutes of CPU time on a single processor of Intel(R) Xeon(R) E5472 (3GHz). The development made in work will greatly facilitate the use of HEOM, an exact and nonperturbative quantum dissipation theory, to the study of realistic systems.

## Acknowledgments

Support from the NNSF of China (21033008 & 21073169), the National Basic Research Program of China (2010CB923300 & 2011CB921400), and the Hong Kong RGC (604709) and UGC (AoE/P-04/08-2) is gratefully acknowledged.

- 
- [1] S. Mukamel, *The Principles of Nonlinear Optical Spectroscopy*, Oxford University Press, New York, 1995.
- [2] S. Mukamel, *Annu. Rev. Phys. Chem.* **51**, 691 (2000).
- [3] T. Brixner, J. Stenger, H. M. Vaswani, M. Cho, R. E. Blankenship, and G. R. Fleming, *Nature* **434**, 625 (2005).
- [4] Y.-C. Cheng and G. R. Fleming, *Annu. Rev. Phys. Chem.* **60**, 241 (2009).
- [5] D. Abramavicius, B. Palmieri, D. V. Voronine, F. Šanda, and S. Mukamel, *Chem. Rev.* **109**, 2350 (2009).
- [6] *Coherent Multidimensional Optical Spectroscopy*, edited by S. Mukamel, Y. Tanimura, and P. Hamm, pages 1207–1469, Special Issue of *Acc. Chem. Res.*, Volume 42, Issue 9, 2009.
- [7] G. S. Engel, T. R. Calhoun, E. L. Read, T. K. Ahn, T. Mančal, Y.-C. Cheng, R. E. Blankenship, and G. R. Fleming, *Nature* **446**, 782 (2007).
- [8] H. Lee, Y.-C. Cheng, and G. R. Fleming, *Science* **316**, 1462 (2007).
- [9] T. R. Calhoun, N. S. Ginsberg, G. S. Schlau-Cohen, Y.-C. Cheng, M. Ballottari, R. Bassi, and G. R. Fleming, *J. Phys. Chem. B* **113**, 16291 (2009).
- [10] G. Panitchayangkoon, D. Hayes, K. A. Fransted, J. R. Caram, E. Harel, J. Z. Wen, R. E. Blankenship, and G. S. Engel, *Proc. Natl. Acad. Sci. USA* **107**, 12766 (2010).
- [11] E. Collini, C. Y. Wong, K. E. Wilk, P. M. G. Curmi, P. Brumer, and G. D. Scholes *Nature* **463**, 644 (2010).
- [12] A. Ishizaki and G. R. Fleming, *Proc. Natl. Acad. Sci. USA* **106**, 17255 (2009).
- [13] S. Mukamel and D. Abramavicius, *Chem. Rev.* **108**, 2073 (2004).
- [14] J. Adolphs and T. Renger, *Biophys. J.* **91**, 2778 (2006).
- [15] D. Abramavicius, D. V. Voronine, and S. Mukamel, *Proc. Natl. Acad. Sci. USA* **105**, 8525 (2008).
- [16] L. P. Chen, R. H. Zheng, Q. Shi, and Y. J. Yan, *J. Chem. Phys.* **132**, 024505 (2010).
- [17] L. P. Chen, R. H. Zheng, Y. Y. Jing, and Q. Shi, *J. Chem. Phys.* **134**, 194508 (2011).
- [18] Y. Tanimura, *Phys. Rev. A* **41**, 6676 (1990).
- [19] Y. Tanimura, *J. Phys. Soc. Jpn.* **75**, 082001 (2006).
- [20] Y. A. Yan, F. Yang, Y. Liu, and J. S. Shao, *Chem. Phys. Lett.* **395**, 216 (2004).
- [21] J. S. Shao, *J. Chem. Phys.* **120**, 5053 (2004).
- [22] R. X. Xu, P. Cui, X. Q. Li, Y. Mo, and Y. J. Yan, *J. Chem. Phys.* **122**, 041103 (2005).
- [23] R. X. Xu and Y. J. Yan, *Phys. Rev. E* **75**, 031107 (2007).
- [24] R. P. Feynman and F. L. Vernon, Jr., *Ann. Phys.* **24**, 118 (1963).
- [25] U. Weiss, *Quantum Dissipative Systems*, World Scientific, Singapore, 2008, 3rd ed. Series in Modern Condensed Matter Physics, Vol. 13.
- [26] H. Kleinert, *Path Integrals in Quantum Mechanics, Statistics, Polymer Physics, and Financial Markets*, World Scientific, Singapore, 2009, 5th ed.
- [27] Y. Tanimura and R. Kubo, *J. Phys. Soc. Jpn.* **58**, 101 (1989).
- [28] J. S. Jin, X. Zheng, and Y. J. Yan, *J. Chem. Phys.* **128**, 234703 (2008).
- [29] Q. Shi, L. P. Chen, G. J. Nan, R. X. Xu, and Y. J. Yan, *J. Chem. Phys.* **130**, 084105 (2009).
- [30] J. Hu, R. X. Xu, and Y. J. Yan, *J. Chem. Phys.* **133**, 101106 (2010).
- [31] J. Hu, M. Luo, F. Jiang, R. X. Xu, and Y. J. Yan, *J. Chem. Phys.* **134**, 244106 (2011).
- [32] J. J. Ding, J. Xu, J. Hu, R. X. Xu, and Y. J. Yan, *J. Chem. Phys.* (2011), accepted.
- [33] R. X. Xu, B. L. Tian, J. Xu, Q. Shi, and Y. J. Yan, *J. Chem. Phys.* **131**, 214111 (2009).
- [34] B. L. Tian, J. J. Ding, R. X. Xu, and Y. J. Yan, *J. Chem. Phys.* **133**, 114112 (2010).
- [35] Y. J. Yan and R. X. Xu, *Annu. Rev. Phys. Chem.* **56**,



- 187 (2005).
- [36] Q. Shi, L. P. Chen, G. J. Nan, R. X. Xu, and Y. J. Yan, *J. Chem. Phys.* **130**, 164518 (2009).
- [37] Note the indexing error in the eq 18 of Ref. [42].
- [38] Y. J. Yan and S. Mukamel, *J. Chem. Phys.* **89**, 5160 (1988).
- [39] Y. J. Yan and S. Mukamel, *J. Chem. Phys.* **94**, 179 (1991).
- [40] S. Mukamel and A. Tortschanoff, *Chem. Phys. Lett.* **357**, 327 (2002).
- [41] S. Mukamel, R. Oszwałdowski, and L. Yang, *J. Chem. Phys.* **127**, 221105 (2007).
- [42] K. B. Zhu, R. X. Xu, H. Y. Zhang, J. Hu, and Y. J. Yan, *J. Phys. Chem. B* **115**, 5678 (2011).